Multinucleon transfer in ^{16,18}O, ^{19}F + ^{208}Pb reactions at energies near the fusion barrier

D. C. Rafferty,* M. Dasgupta, D. J. Hinde, C. Simenel, E. C. Simpson, E. Williams, I. P. Carter, K. J. Cook, D. H. Luong, S. D. McNeil, K. Ramachandran,† K. Vo-Phuoc, and A. Wakhle‡

Department of Nuclear Physics, Australian National University, Canberra, Australia

(Received 14 June 2016; published 10 August 2016)

Background: Nuclear reactions are complex, involving collisions between composite systems where many-body dynamics determines outcomes. Successful models have been developed to explain particular reaction outcomes in distinct energy and mass regimes, but a unifying picture remains elusive. The irreversible transfer of kinetic energy from the relative motion of the collision partners to their internal states, as is known to occur in deep inelastic collisions, has yet to be successfully incorporated explicitly into fully quantal reaction models. The influence of these processes on fusion is not yet quantitatively understood.

Purpose: To investigate the population of high excitation energies in transfer reactions at sub-barrier energies, which are precursors to deep inelastic processes, and their dependence on the internuclear separation.

Methods: Transfer probabilities and excitation energy spectra have been measured in collisions of ^{16,18}O, ^{19}F + ^{208}Pb, at various energies below and around the fusion barrier, by detecting the backscattered projectile-like fragments in a ΔE-E telescope.

Results: The relative yields of different transfer outcomes are strongly driven by Q values, but change with the internuclear separation. In ^{16}O + ^{208}Pb, single nucleon transfer dominates, with a strong contribution from $-2p$ transfer close to the Coulomb barrier, though this channel becomes less significant in relation to the $-2p2n$ transfer channel at larger separations. For ^{18}O + ^{208}Pb, the $-2p2n$ channel is the dominant charge transfer mode at all separations. In the reactions with ^{19}F, $-3p2n$ transfer is significant close to the barrier, but falls off rapidly with energy. Multinucleon transfer processes are shown to lead to high excitation energies (up to ∼15 MeV), which is distinct from single nucleon transfer modes which predominantly populate states at low excitation energy.

Conclusions: Kinetic energy is transferred into internal excitations following transfer, with this energy being distributed over a larger number of states and to higher excitations with increasing numbers of transferred nucleons. Multinucleon transfer is thus a mechanism by which energy can be dissipated from the relative motion before reaching the fusion barrier radius.

DOI: 10.1103/PhysRevC.94.024607

I. INTRODUCTION

The coupled-channels model describes cross sections for both peripheral reactions and fusion by considering the colliding nuclei to be in a coherent superposition of their intrinsic states [1]. This approach has been highly successful at reproducing the observed fusion enhancement in the vicinity of the Coulomb barrier across many systems, and has demonstrated the importance of couplings between the internuclear motion and internal excitations in the reactants [2,3]. Though highly successful in the near-barrier region, and offering important insights into the physical mechanisms underlying fusion reactions, several studies have demonstrated that standard implementations of the coupled-channels formalism are not always adequate [4–6]. In particular it has been suggested that important dynamic effects are not being properly accounted for [7–9].

Discrepancies are observed both above [7,8] and far below [4,7,10,11] the Coulomb barrier, with coupled channels models overpredicting cross sections compared to experimental data. At energies above the Coulomb barrier, fusion hindrance was suggested to be due to irreversible dissipation of energy from the relative motion to internal excitations [6], lowering the probability for overcoming the barrier. This idea is taken from the much studied phenomenon of deep inelastic scattering, where it is accepted that a major rearrangement of nucleons between the reactants reduces the kinetic energy in the system and so hinders fusion [12]. Studies of deep sub-barrier fusion hindrance have shown that the effect can be reproduced by modifying the potential or couplings used in the calculations [4,13]. However, these approaches do not address self-consistently the problems at above barrier energies [5,7].

The transition between the deep inelastic scattering phenomenon, expected at above-barrier energies, and the quasielastic and quantum tunneling regime below the barrier remains poorly understood [14,15]. It has been suggested that at low energies irreversible energy loss can proceed through doorway states such as giant resonances [16] and cluster transfer [17], which may occur even at large internuclear separation. Understanding the transition between the quasielastic and deep-inelastic scattering regimes in detail is an important step towards developing a complete picture of energy dissipation in both peripheral reactions and fusion.

*dominic.rafferty@anu.edu.au

†Present address: Nuclear Physics Division, Bhabha Atomic Research Centre, Mumbai, India.

‡Present address: National Superconducting Cyclotron Laboratory, Michigan State University, East Lansing, MI, USA.

Few-nucleon transfer reactions provide an important tool for studying this transition [18], as these channels span the range of energies between the sub-barrier and the complex (dissipative) deep inelastic regimes, and are expected to evolve smoothly between them. Of particular interest are those channels that lead to high excitation energies in the outgoing fragments, which can in principle suppress fusion.

In this work, we have measured the probabilities of different single- and multinucleon transfer channels in reactions involving light nuclei including their evolution as a function of the internuclear separation. An additional focus of the work has been to evaluate the excitation energy distributions for each transfer mode to investigate how the dissipation of energy from the relative motion might occur through these, and in multinucleon transfer in general.

II. EXPERIMENT

Measurements were made at the Australian National University Heavy Ion Accelerator Facility, where beams of ^{12,13}C, ^{16,18}O, and ^{19}F from the 14UD tandem electrostatic accelerator were produced in the energy range 3.5–5 MeV/A, corresponding to 90–100 % of the capture barrier energy V_B in the colliding systems. The beams were incident on a target of ^{208}PbS of thickness 80 μg cm^{-2}, supported by a carbon backing of thickness 15 μg cm^{-2}. The range of bombarding energies $E_{\rm c.m}$ and fusion barrier energies V_B of the systems of interest are listed in Table I. In this and the following discussion, center-of-mass energies $E_{\rm c.m}$ are reported having been corrected for energy losses of the beam and reaction products in the target calculated using SRIM [19].

There are two standard methods which have been widely used to measure transfer probabilities as a function of internuclear separation—measuring angular distributions at a fixed energy, or alternatively measuring excitation functions at fixed backward angles at sub-barrier energies [15]. In this experiment we have pursued the latter—back-scattered projectile-like fragments (PLFs) were detected at a laboratory angle $\theta_{\rm lab} = 160.6^\circ$ using a ΔE-E telescope, with yields normalized to Rutherford scattering events in two forward angle monitor detectors at $\theta_{\rm lab} = \pm 22.5^\circ$ to give absolute probabilities of the identified channels. The experimental setup is schematically shown in Fig. 1.

TABLE I. Fusion barrier and beam energies (both in the center-of-momentum frame) in systems studied in this work. The capture barrier for ^{16}O + ^{208}Pb is the average barrier energy extracted from the measured experimental barrier distribution [20]. The values for ^{18}O + ^{208}Pb and ^{19}F + ^{208}Pb are scaled according to the masses and charges of the light projectile.

System	Barrier energy V_B (MeV)	Beam energies $E_{\rm c.m.}$ (MeV)
^{16}O + ^{208}Pb	74.5	73.0, 72.5, 70.9, 69.3
^{18}O + ^{208}Pb	73.6	73.6, 71.6, 71.1, 70.3, 69.6, 68.0
^{19}F + ^{208}Pb	82.4	83.3, 81.3, 80.6, 78.9, 77.2, 75.5, 74.1

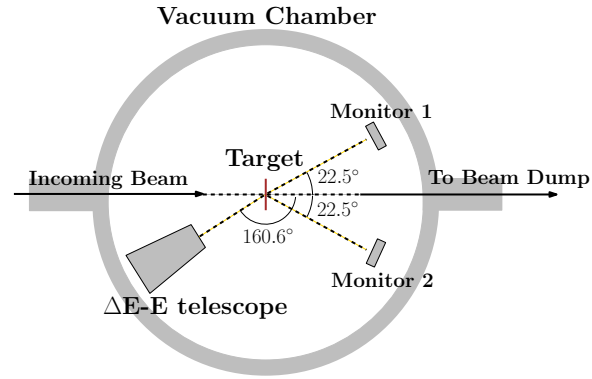

FIG. 1. Schematic diagram of the experimental setup. The monitor detectors are placed perpendicular to the plane containing the ΔE-E telescope.

The ΔE-E telescope used in this experiment consisted of a Frisch grid ionization chamber [21], which measures the energy lost by the incoming ion ΔE in a propane gas volume, and the residual energy $E_{\rm Si}$ in a silicon detector. Reaction products are separated in mass and charge due to their differing stopping powers and thus energy loss in the gas. The sub-barrier energies of interest and the backward angle of the detector limit the energy that can be deposited in the ΔE detector to relatively small values (15–30 MeV), requiring low electronic noise. From the measured quantities, after correcting for energy losses in the ΔE detector window and silicon detector dead layer, we can derive the Q-value distributions of products arising from the different processes. This allows us to examine the transfer of energy from the relative motion to internal excitation of the reactants.

Typical ΔE-$E_{\rm Si}$ spectra are shown in Fig. 2 for the three reactions of interest at a bombarding energy equivalent to 0.98 V_B. The reaction products are separated into groups according to charge, with a finer structure visible within these groups corresponding to different mass isotopes. For example, in Fig. 2(a), the carbon group exhibits two intense bands corresponding to the isotopes ^{12,14}C. An intense band of events identified as α particles was observed for all measurements at low ΔE values, which was used to aid the calibration of the detector.

III. ANALYSIS

The main challenge in identifying reaction products is in determining the unique locii in the ΔE-E spectrum belonging to each isotope. For this purpose, projectiles corresponding to products of interest were back-scattered from a thick tantalum target. The projectiles can scatter at various depths in the target, and thus emerge over a wide energy range as shown in Fig. 3, where the spectra obtained from elastic back-scattering of ^{12}C, ^{18}O, and ^{19}F from the thick target are superimposed. This allows us to map out the locii of the different isotopes in the ΔE-E spectrum, which remain constant throughout of the experiment as long as the detector properties (biases and gas pressure) are unchanged. These measurements were made at energies well below the barrier to ensure that nearly all events seen in the detector correspond to elastic scattering.

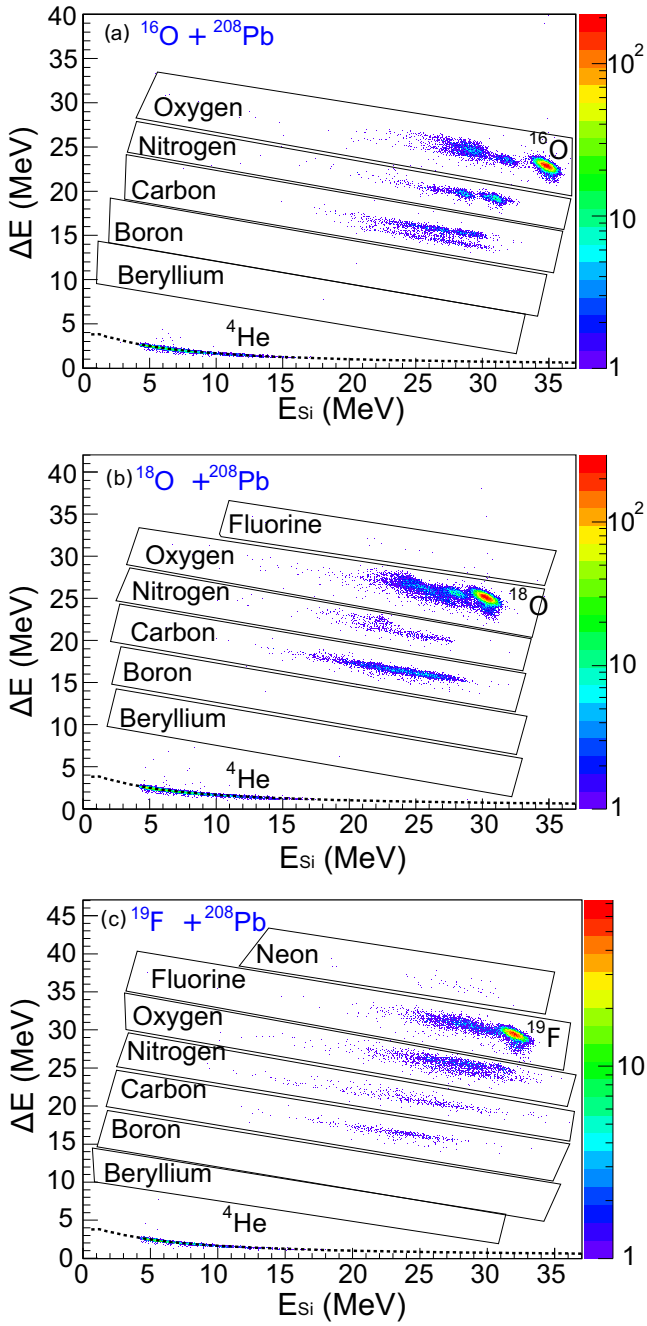

FIG. 2. ΔE-E_{Si} spectra obtained for (a) $^{16}\mathrm{O} + ^{208}\mathrm{Pb}$, (b) $^{18}\mathrm{O} + ^{208}\mathrm{Pb}$, (c) $^{19}\mathrm{F} + ^{208}\mathrm{Pb}$ at $E_{\mathrm{c.m.}}/V_B \approx 0.98$. Main intense spots correspond to elastically scattered beam species. Products are shown to be well separated in charge, with the carbon band also showing separation of species by mass. Black dashed lines are SRIM [19] calculations showing the expected locus of α particles in the ΔE-E telescope. In the $^{18}\mathrm{O} + ^{208}\mathrm{Pb}$ (b) and $^{19}\mathrm{F} + ^{208}\mathrm{Pb}$ (c) reactions, we observe a small number of events corresponding to charge pickup by the projectile. However, the vast majority of events correspond to charge stripping from the projectile, elastic/inelastic scattering, and neutron transfer reactions.

Once the locii have been identified, isotopes within each band can be separated by finding the relative energy loss ΔE_{rel} in the ionisation chamber of all events relative to the nearest

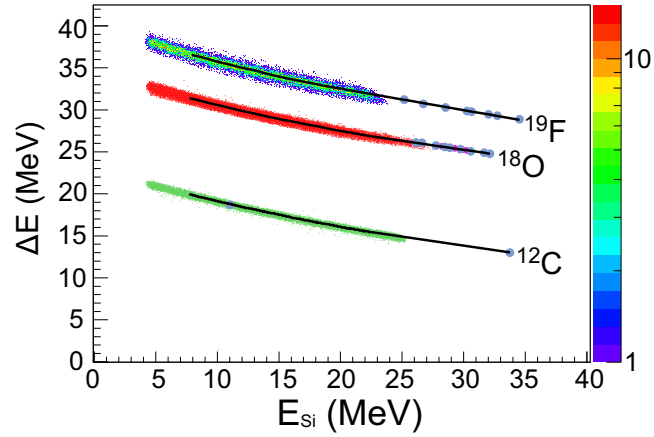

FIG. 3. Mapping of ^{12}C, ^{18}O, and ^{19}F locii in the ΔE-E_{Si} spectrum. The intense bands of events are from scattering of each projectile from a thick tantalum target. The positions of the elastic peaks for scattering of each projectile from the thin Pb target are indicated by the blue circles, and are used to map the locii to higher energies. The locii determined through this method are shown in the figure by the solid black lines. The intensity scale on the right of the figure applies only to the ^{19}F band.

identified locus. An example is shown in Fig. 4(a), where the identified locus of ^{12}C is overlaid on the measured ΔE-E_{Si} spectra for $^{16}\mathrm{O} + ^{208}\mathrm{Pb}$ at 0.99 V_B. Here we have defined ΔE_{rel} as the deviation in ΔE with respect to the locus of ^{12}C. The resulting ΔE_{rel} distribution is shown in Fig. 4(b), and is analysed through a process of Gaussian deconvolution. The peak widths of all isotopes of the same element are taken to be equal, which reduces the number of parameters of the fit. The best fit was found by minimizing χ^2 with respect to the number of peaks, whilst constraining the width to be consistent with the expected systematics (derived from the elastic scattering peaks for the various beam-species). The yields of each product are then found by taking the integrals of the individually separated Gaussian components. Once the yields have been determined, they are normalised to Rutherford scattering events in the forward angle monitor detectors, giving absolute probabilities for each reaction channel [5,22].

To obtain Q-value and excitation energy spectra, gates were applied to the ΔE_{rel} spectra to identify products on an event-by-event basis. These are guided by the mapped species locii, with adjacent isotopes separated by mapping the edges of the gates to the intersections between the adjacent fitted Gaussian components, as shown by the vertical dashed lines in Fig. 4(b). This method was chosen to give optimal isotopic identification of each event, and to provide minimal mixing of adjacent isotopes.

After identification of the projectile-like fragments, the Q-value spectrum of the reaction can be reconstructed by tracing back to the center-of-mass system on an event-by-event basis from the known beam energy and measured final energies. The Q value is calculated according to

$$Q = \frac{A_3 + A_4}{A_4} E_3 - \frac{A_4 - A_1}{A_4} E_1 - \frac{2\sqrt{A_1 A_3 E_1 E_3}}{A_4} \cos\theta_{\mathrm{lab}}. \quad (1)$$

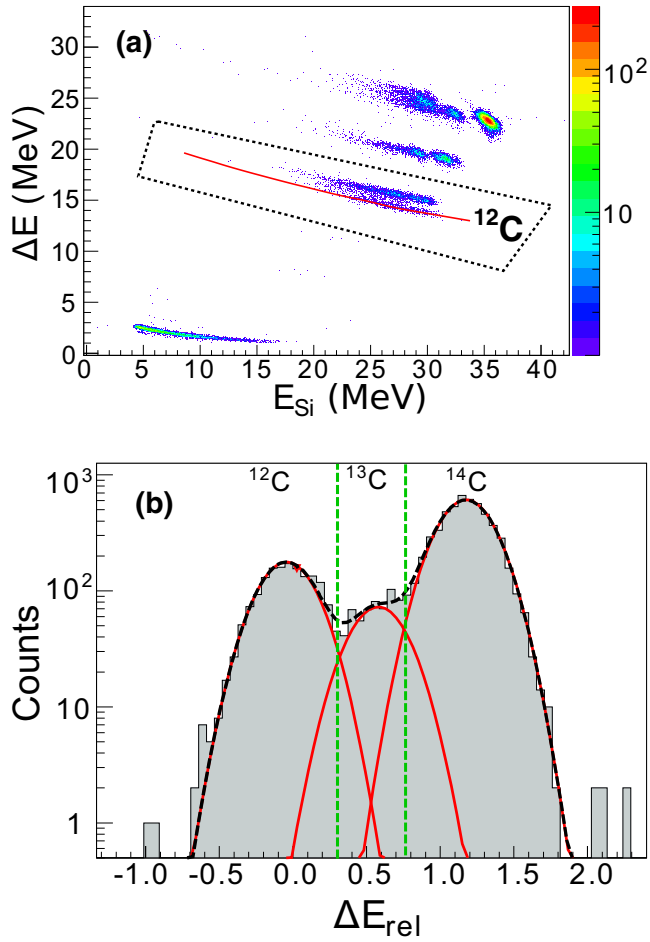

FIG. 4. (a) ΔE-$E_{\rm Si}$ plot obtained in the reaction ^{16}O + ^{208}Pb at 0.98 V_B. The red line shows the ^{12}C locus from which the relative energy loss ($\Delta E_{\rm rel}$) spectrum is calculated. The $\Delta E_{\rm rel}$ spectrum is determined from events within the dashed contour. (b) Resulting $\Delta E_{\rm rel}$ spectrum. Red curve shows the multiple Gaussian function fitted to the distribution. Black curves indicate the corresponding fitted components, which are attributed to yields of the expected isotopes, in this case ^{12,13,14}C. Vertical blue dashed lines show the gate limits for event-by-event analysis as determined by the intersections between adjacent fitted peaks.

In the above, subscripts are given in the standard reaction notation 2(1,3)4, where 1 is the projectile, 2 the target, 3 the ejectile, and 4 the recoiling target-like nucleus, with A_i their masses and $\theta_{\rm lab}$ the scattering angle in the laboratory frame. E_i are the energies, with E_1 the projectile energy, and E_3 the measured energy of the detected projectile-like product, after correction for energy losses in the target and detector dead layers. From the deduced Q value and knowledge of the identity of each event, we can deduce the excitation energy of the reaction products according to

$$E_x = Q_{\rm g.g.} - Q, \tag{2}$$

where $Q_{\rm g.g.}$ is the ground-state to ground-state transfer Q value, and Q is that given by Eq. (1).

IV. Q-VALUE DEPENDENCE OF TRANSFER PROBABILITIES

Multinucleon transfer cross sections have been shown to have an approximately exponential dependence on the reaction Q value [23,24], with the cross sections for production of each element lying on parallel lines, shifted relative to each other according to the difference in the Coulomb potential between the entrance and exit channels. Correcting the ground-state Q values by the change in the Coulomb potential, evaluated at the distance of closest approach, gives an effective Q value $Q_{\rm eff} = Q_{\rm g.g.} - \Delta V_C$, with ΔV_C the Coulomb energy shift. This provides a rough basis for estimating the relative strength of different channels. The Q values $Q_{\rm g.g.}$ for the ground-state–to–ground-state transfer processes and the $Q_{\rm eff}$ (incorporating the relevant ΔV_C) are listed in Table II in the Appendix for all likely transfer modes in the three systems studied.

The correlation between the transfer probabilities at around 95% of the barrier energy and the corresponding effective Q values is shown in Fig. 5(a)–5(c) for each collision pair. Viewed this way, there is no clear dependence of the channel probability on the effective Q value. In each case a large number of transfer processes are observed. In general, single-nucleon transfers are strong, though in the case of ^{18}O $-2p2n$ is found to be the most significant, with other complex transfer channels such as $-1p2n$ and $-2p3n$ being stronger than single proton stripping.

In Fig. 5(d)–5(f) we demonstrate, however, an exponential correlation between these quantities when we consider together channels of the same charge transfer. The correlation appears strongest in the case of the $\Delta Z = -1$ channels, though the probabilities where two and three charges are transferred also suggest this broad trend. For a given number of protons transferred, the probability is strongly driven by Q-value effects, while the number of neutrons also transferred is largely irrelevant. Similar conclusions can be drawn when comparing the measured probabilities at other values of $E_{\rm c.m.}/V_B$.

V. RADIAL SEPARATION DEPENDENCE

To obtain a full picture of the effects of transfer on fusion and its relation to the dissipation of kinetic energy from the relative motion, it is important to understand the energy dependence of these processes. This allows us to build an idea of what processes occur in the barrier region as well as at large separations that might have a bearing on the fusion mechanism. Furthermore the energy dependence is required for extrapolation of the transfer probabilities to the barrier radius for use in phenomenological models [25,26] which include transfer channels.

A. Quasielastic scattering and total transfer probability

Here we consider the global behavior of the reflected flux for the three reactions under study, and how it varies with internuclear separation. In order to compare different reactions, the surface separation parameter Δ is used, as it eliminates the dependence on the reactant masses [27–29].

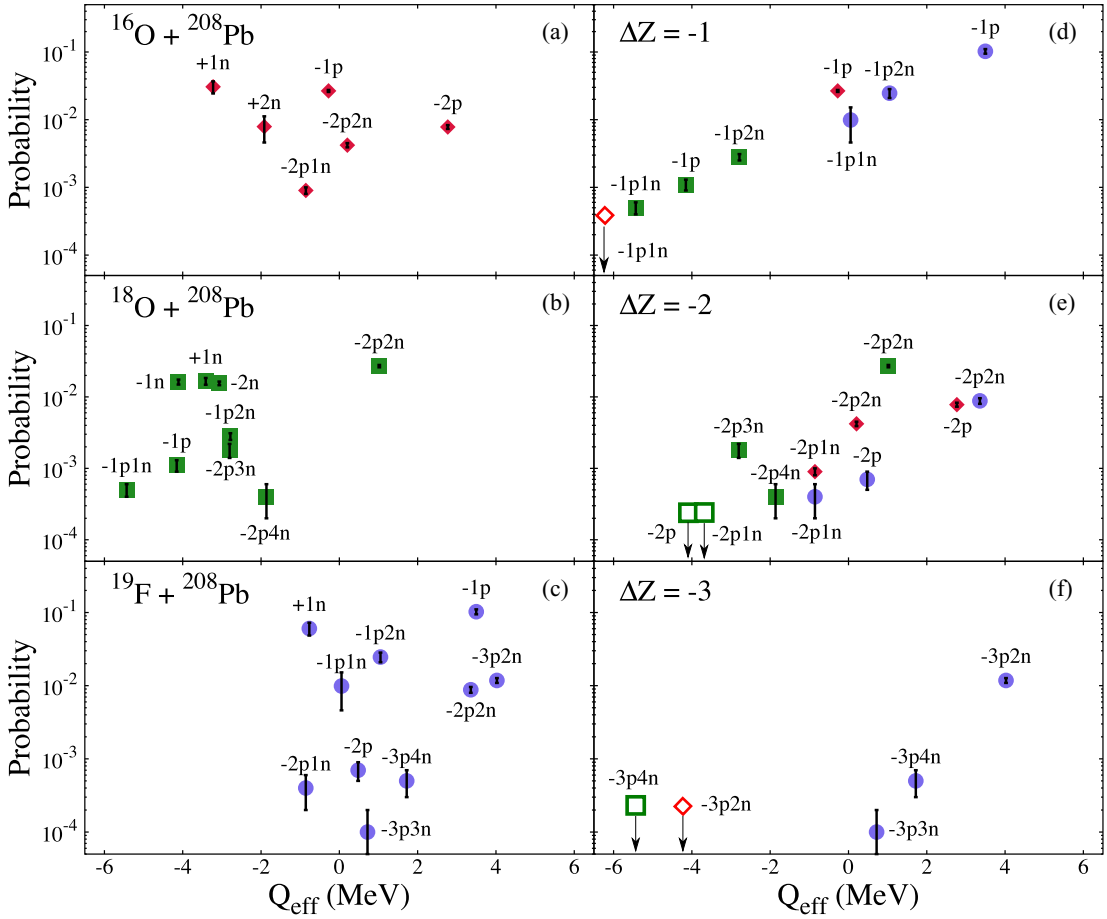

FIG. 5. Measured probabilities at $E_{\mathrm{c.m}} \sim 0.95V_B$ for various transfer processes in the studied reactions and the associated effective Q values, corresponding to the data shown in Table II. Left hand panels (a–c) show the data for the reactions indicated. Right hand panels (d—f) show the data sorted by ΔZ channel. The downward arrows indicate all of the modes that are within the shown range in Q_{eff} but are not observed experimentally, thus their probabilities are much closer to zero.

This is given by

$$\Delta = r_{\mathrm{min}} - r_0\left(A_p^{1/3} + A_t^{1/3}\right), \tag{3}$$

where the subscripts p and t represent the projectile and target, respectively. r_0 above is the nuclear matter radius parameter in the sharp cutoff model, for which we have used the standard value of 1.2 fm [30]. r_{min} is the distance of closest approach of the reactants assuming pure Coulomb classical trajectories [see Appendix Eq. (A2)].

The total quasielastic scattering cross section (elastic + inelastic + transfer) as a fraction of that for Rutherford scattering is shown in Fig. 6(a). The total probability for transfer as a function of the surface separation is shown in Fig. 6(b). As the internuclear separation is reduced there is a corresponding reduction in the quasielastic flux due to increased fusion. At large distances, the total transfer probability depends exponentially on the internuclear separation. The total transfer probability increases as Δ is reduced before saturating near the barrier energy, where it is ∼50% of the total. Though the transfer probability saturates, the quasielastic cross section continues to fall, such that the transfer channels become an increasingly large fraction of the backscattered flux.

The systematic trends are broadly the same for all three reactions. The ^{19}F-induced reaction has a markedly higher probability for transfer than those of ^{16,18}O. As will be shown later in Fig. 9, single proton stripping from the fluorine projectile is the dominant transfer mode in ^{19}F + ^{208}Pb. It is shown in Fig. 6(b) that excluding this mode in the sum of probabilities reconciles the fluorine data with that of the oxygen isotopes at smaller separations, though a discrepancy remains at larger values. This difference in the transfer behavior of fluorine is likely associated with the single proton outside the $Z = 8$ shell. Despite this difference, the total quasielastic flux is very similar to the other reactions. Not only are a large number of multinucleon transfer channels observed, but they also represent a large fraction of the backscattered flux close to the barrier energy.

B. Semiclassical transfer

Before examining the radial dependence of the transfer probabilities of individual channels, we first discuss some of the expectations from the viewpoint of semiclassical models [31]. The details of the theory are outlined in the Appendix. The transfer probability is expected to depend exponentially

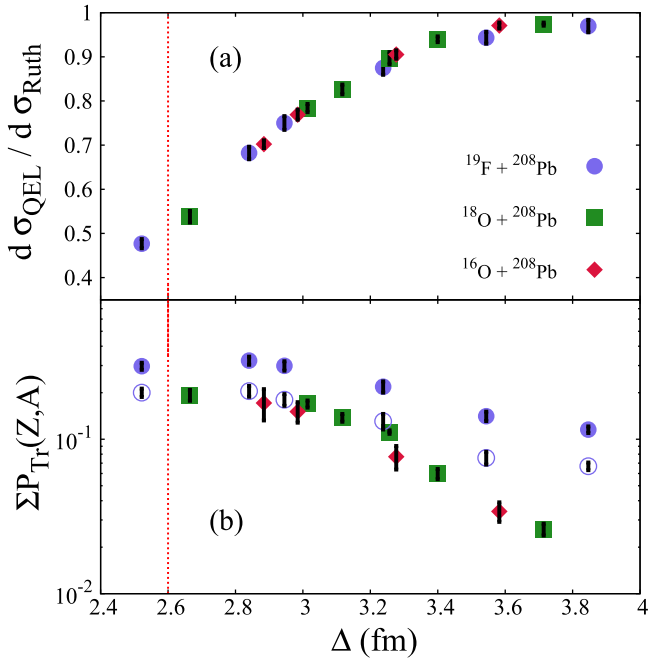

FIG. 6. (a) Ratio of the quasielastic and Rutherford scattering cross sections for all systems as a function of the surface separation parameter Δ. (b) Total transfer probability for each system. Key shown in the top panel is relevant to both panels. Open circles in the bottom panel show the sum of channel transfer probabilities in $^{19}F + ^{208}Pb$ excluding the $-1p$ channel. Vertical red dashed line indicates the approximate location of the fusion barrier in the Δ coordinate, where the probability for absorption = 0.5.

on the distance of closest approach r_{min}:

$$P_{Tr}(r_{min}) \propto \exp(-2\alpha r_{min}), \tag{4}$$

where the slope parameter α is related to the binding energies of the transferred nucleons in the donor and acceptor nuclei. Further details, and fitted values of the slope parameters α_{exp} can be found in the Appendix.

When considering multinucleon transfer, in the simplest picture the slope parameter should scale with the number of nucleons transferred (i.e., $\alpha_{2n} \simeq 2\alpha_{1n}$), with the absolute probability scaling accordingly. For example,

$$P_{2n} \simeq (P_{1n})^2. \tag{5}$$

This scaling, together with Eq. (4), suggests that at low energies, with larger internuclear separations, simple single nucleon transfer channels should be most important. As the energy increases and the barrier is approached, multinucleon transfer modes are likely to become more important.

Enhancements relative to this expectation have commonly been attributed to correlations beyond the simple model. Fully microscopic calculations based on the independent particle picture have shown that Eq. (5) serves only as an approximation to sequential nucleon transfer [17,32]. In addition, the inclusion of pairing correlations [33], quantum fluctuations [34,35] and particle evaporation [36] leads to a more complicated picture.

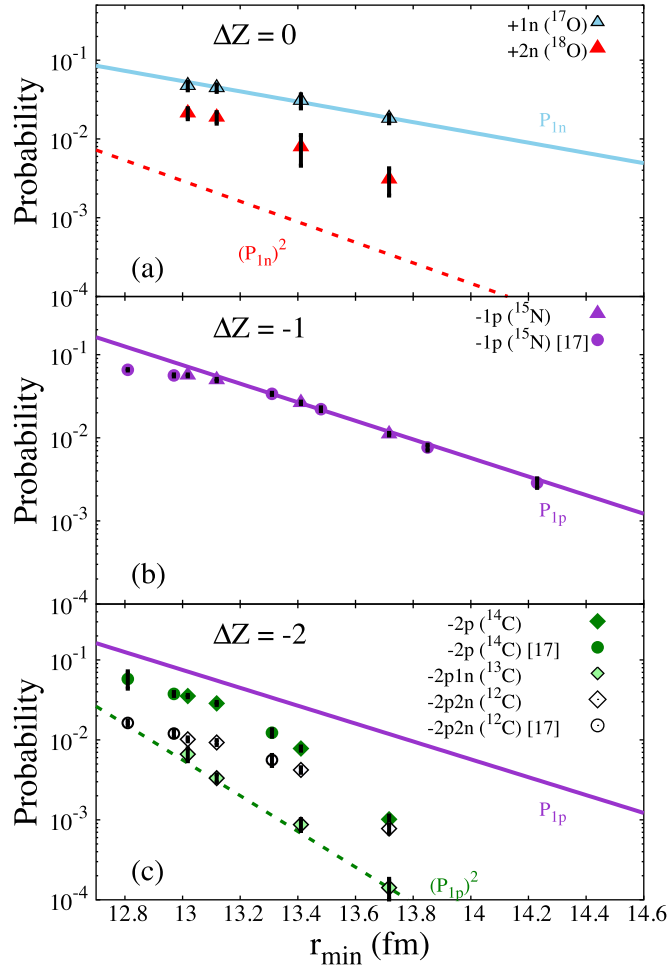

FIG. 7. (a) Measured one and two neutron pickup probabilities. Blue line is a fit to the 1n transfer data ($\Delta N = +1$), and the red dashed line is the expected pickup of two independent neutrons ($\Delta N = +2$) according to Eq. (5). (b) One proton stripping probability as a function of the separation (triangles), along with those reported in Ref. [17] (circles). The purple line is a fit to the data in the range 13.1 fm $\leqslant r_{min} \leqslant$ 14.5 fm. (c) Measured $\Delta Z = -2$ channels in this experiment (diamonds), along with those reported in Ref. [17] (circles). Shown again is the fit to the $1p$ stripping data shown in (b), along with its square (green dashed line), which is the expected probability of stripping of two independent protons according to Eq. (5).

C. Results for $^{16}O + ^{208}Pb$

Multinucleon transfer at sub-barrier energies in the $^{16}O + ^{208}Pb$ system has been the focus of several previous studies [17,37–39]. With the enhanced mass resolution of the new ΔE-E detector used in the present experiment, we have measured this system again in order to clarify the trends of the two charge stripping channels, and to extend these measurements to lower energies (larger r_{min}).

Figure 7 shows the most significant transfer channels identified in the $^{16}O + ^{208}Pb$ system, along with the results of the previous ANU experiment [17]. Figure 7(a) shows neutron transfer, with transfer of one and two neutrons from the target to the projectile being seen in the experiment. The blue line is a fit to the $1n$ data, and the red dashed line is the square of

this, which is expected to correspond to a sequential transfer of two neutrons according to Eq. (5). The measured two neutron transfer is shown to exceed the square of the fitted 1n data by around an order of magnitude, though is in agreement with the expected slope of the transfer function.

Figure 7(b) shows $\Delta Z = -1$ products, in which the only ejectile significantly populated is ^{15}N, associated with single proton transfer. Other $\Delta Z = -1$ products are too weak to separate in this reaction. Figure 7(c) shows $\Delta Z = -2$ products. The $2p$ transfer exceeds the prediction of Eq. (5) (green dashed line). The $1p$ trend is indicated by the purple line for comparison. At the highest energies (smallest $r_{\min}$) the $2p$ transfer is comparable in strength to $1p$ transfer, and is in agreement with time-dependent Hartree-Fock predictions [40]. The $2p2n$ transfer also far exceeds the expectation of Eq. (5), and is stronger than $2p1n$ transfer. Of particular note is the behavior of the $2p$ and $2p2n$ channels as the internuclear separation increases, where their probabilities become almost equal. Extrapolating to larger distances, it appears likely that the $-2p2n$ channel producing ^{12}C will become dominant over that producing ^{14}C. In the previous experiment with a similar experimental set-up [17], the dominance of $-2p$ over $-2p2n$ transfer was reported, but with an improved mass resolution we can elucidate the low energy behavior. At the fusion barrier the strongest channels are one nucleon stripping, followed by two-nucleon and $2p2n$ stripping.

D. Results for ^{18}O + ^{208}Pb

Figure 8 shows the measured transfer probabilities in the ^{18}O + ^{208}Pb system. In Fig. 8(a), we show the experimental data for the observed $-1n$ and $-2n$ transfer. The probability for $2n$ transfer is comparable to that of $1n$ neutron transfer. This behavior has been observed previously in several reactions involving ^{18}O [41,42], and is thought to be due to the valence dineutron configuration in this nucleus, where the two neutrons outside the closed shell are weakly bound and easily removed. It is likely that the $-2n$ transfer is underestimated here, as it is difficult to separate the ^{16}O yield arising from ground-state transfer from elastic scattering events, as there is some overlap in the ΔE-$E_{\rm Si}$ spectrum. The probabilities for transfer of a single neutron in either direction (pickup or stripping) appear to be very similar, as might be expected due to their similar Q values (-3.412 and -4.108 for pickup and stripping, respectively). For comparison, the measured trends for $-2p2n$ (the strongest transfer mode) and $-1p$ are shown by the dashed green and solid purple lines, respectively.

Figure 8(b) shows the mass partitions associated single proton stripping. $1p$ stripping is comparatively weak in this reaction, with the $1p2n$ transfer mass partition the most intense of the $\Delta Z = -1$ modes at all separations. Similar behavior in ^{18}O has been reported elsewhere [42], and was interpreted as being due to a correlated transfer of the three nucleons. However, as the internuclear separation is increased, this effect appears to be diminished, with the $-1p2n$ channel nearing equivalence to proton transfer at the lowest energy measured here. The $-2p2n$ trend is plotted here to emphasize the extent to which this transfer mode exceeds all of the $\Delta Z = -1$ channels.

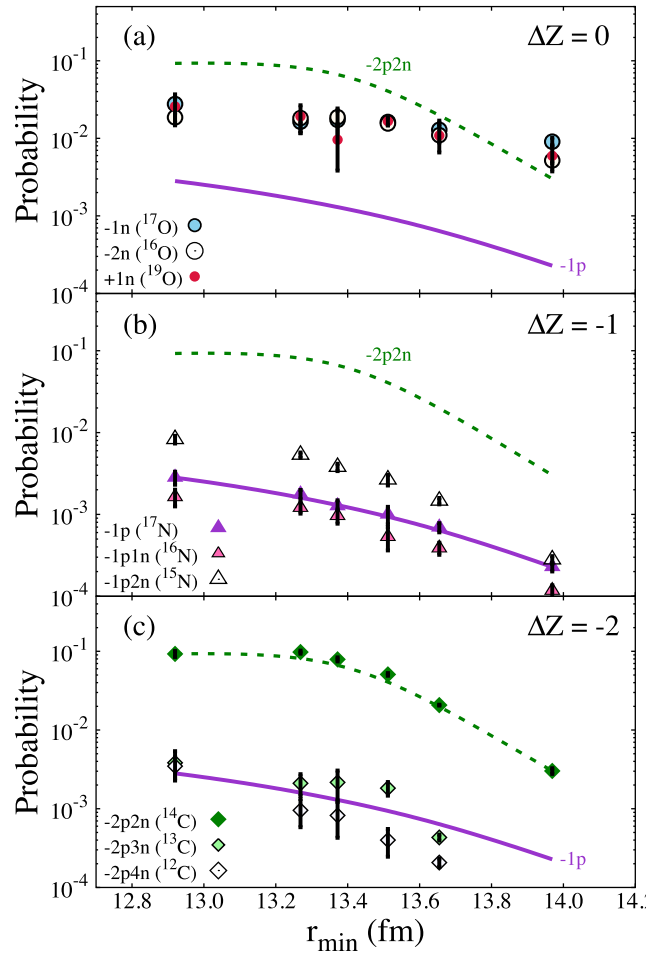

FIG. 8. (a) shows measured neutron transfer probabilities. We show also the trends in the $-1p$ and $-2p2n$ (α) modes for the sake of comparison by the solid purple and dashed green lines respectively. (b) shows measured probabilities for channels involving the transfer of one proton, again with the $-2p2n$ and $-1p$ trends for comparison. (c) shows $\Delta Z = -2$ channels, along with the measured $-1p$ and $-2p2n$ trends.

Figure 8(c) shows the data for $\Delta Z = -2$. The $-2p2n$ channel is dominant over all others involving charge transfer in this system, over the entire energy range studied. The transfer products of $2p3n$ and $2p4n$ are weak, though comparable to $1p$ transfer, which is indicated by the full (purple) line.

E. Results for ^{19}F + ^{208}Pb

Transfer probabilities for ^{19}F + ^{208}Pb are shown in Fig. 9. In Fig. 9(a), we show the data for $1n$ and $1p$ pickup. Neutron pickup, forming ^{20}F, is reasonably strong in this reaction, being comparable to $1p$ stripping, which is the strongest transfer mode, indicated in this panel by the full (blue) line. Charge pickup is present in this reaction, with a small yield of $Z = 10$ events observed at all bombarding energies. Several $\Delta Z = +1$ channels have positive Q values in this system, as shown in Table II (see Appendix). We do not have sufficient statistics to conclusively separate these events by mass, though the $1p2n$ pickup mode has the most favorable Q-value conditions (see

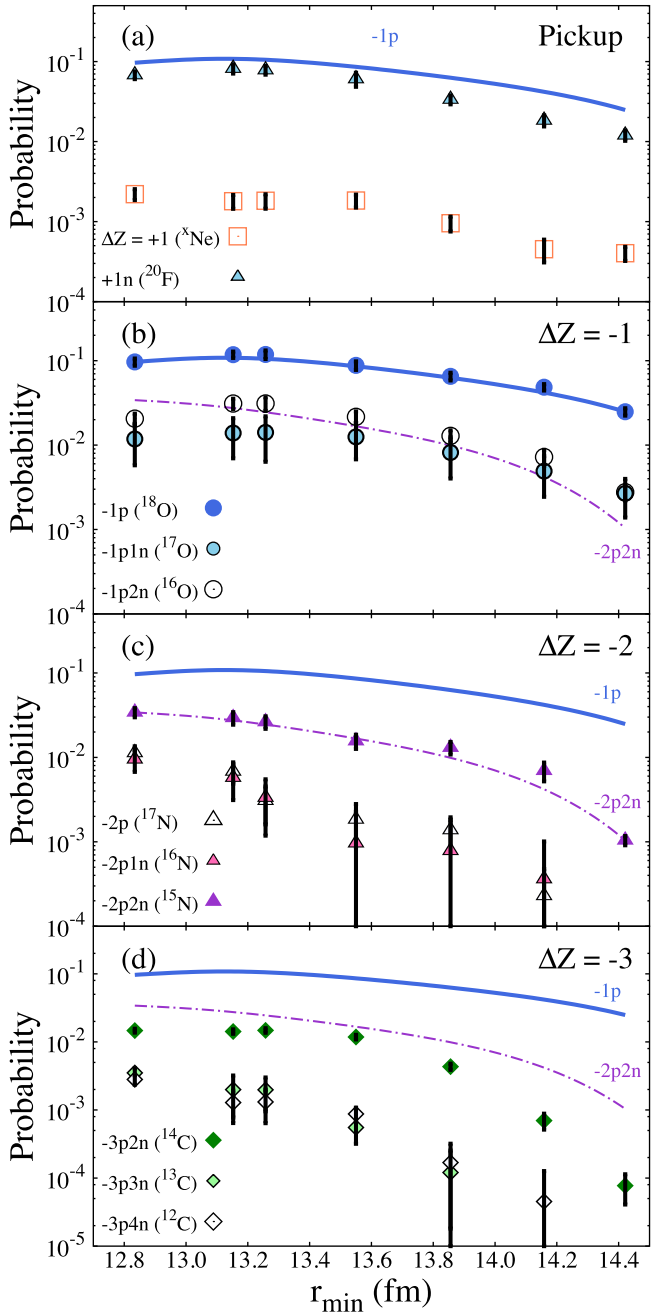

FIG. 9. (a) One proton and one neutron pickup probabilities. Note that we cannot unambiguously separate the neon products, so the square symbols represent the total $\Delta Z = +1$ probabilities. (b) Measured $\Delta Z = -1$ probabilities. Solid blue line and dashed blue line indicate $-1p$ and $-1p2n$ trends to guide the eye. (c) $\Delta Z = -2$ probabilities. Shown also are the trend lines of the most significant $\Delta Z = -1$ modes for comparison, with the trend in $-2p2n$ indicated by the purple dash dotted line. (d) $\Delta Z = -3$ probabilities, along with the most significant $\Delta Z = -1$ and $\Delta Z = -2$ trends for comparison.

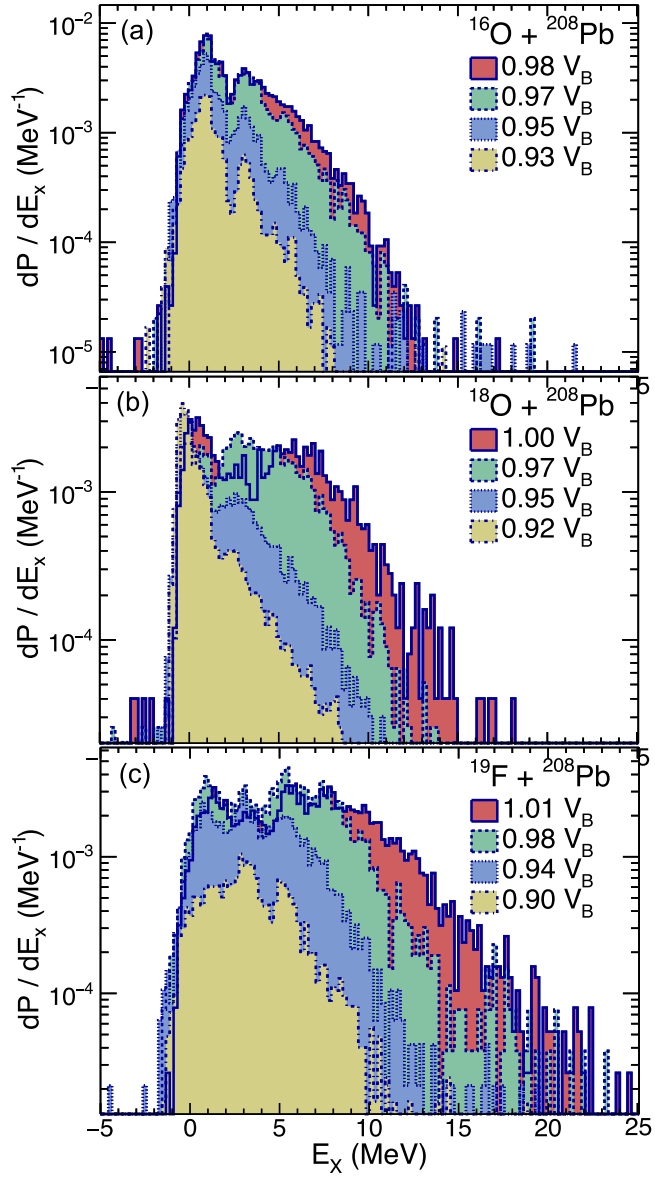

FIG. 10. Variation in the distribution of excitation energy following transfer reactions in $^{16}\mathrm{O} + ^{208}\mathrm{Pb}$ (a), $^{18}\mathrm{O} + ^{208}\mathrm{Pb}$ (b), and $^{19}\mathrm{F} + ^{208}\mathrm{Pb}$ (c). Legend labels give bombarding energies in the center-of-momentum frame $E_{\mathrm{c.m.}}$ as a factor of the barrier energy V_B.

Table II in the Appendix). In this system, one proton stripping is by far the strongest mode involving charge transfer.

Figure 9(b) shows $\Delta Z = -1$ transfer modes. We observe the production of ^{16,17,18}O, with single proton transfer being strongest. Significantly, $-1p2n$ transfer is stronger than $-1p1n$ over the entire range of distances except in the lowest energy measurement.

Figure 9(c) shows $-2p2n$ transfer to be the most significant $\Delta Z = -2$ mode, which also exceeds all $\Delta Z = -1$ channels other than single proton stripping. The $-1p$ transfer trend is indicated by the solid blue line for comparison. We see very few events corresponding to $2p$ or $2p1n$ transfer: In fact ^{15}N has a significantly more favorable Q value and is produced with by far the highest abundance of all nitrogen isotopes. This may also be in part due to the low neutron separation thresholds in ^{17}N (5.88 MeV) and ^{16}N (2.49 MeV), meaning a contribution from evaporation to the high ^{15}N yield. However, any such contribution is likely to be very small on the basis of Q-value considerations.

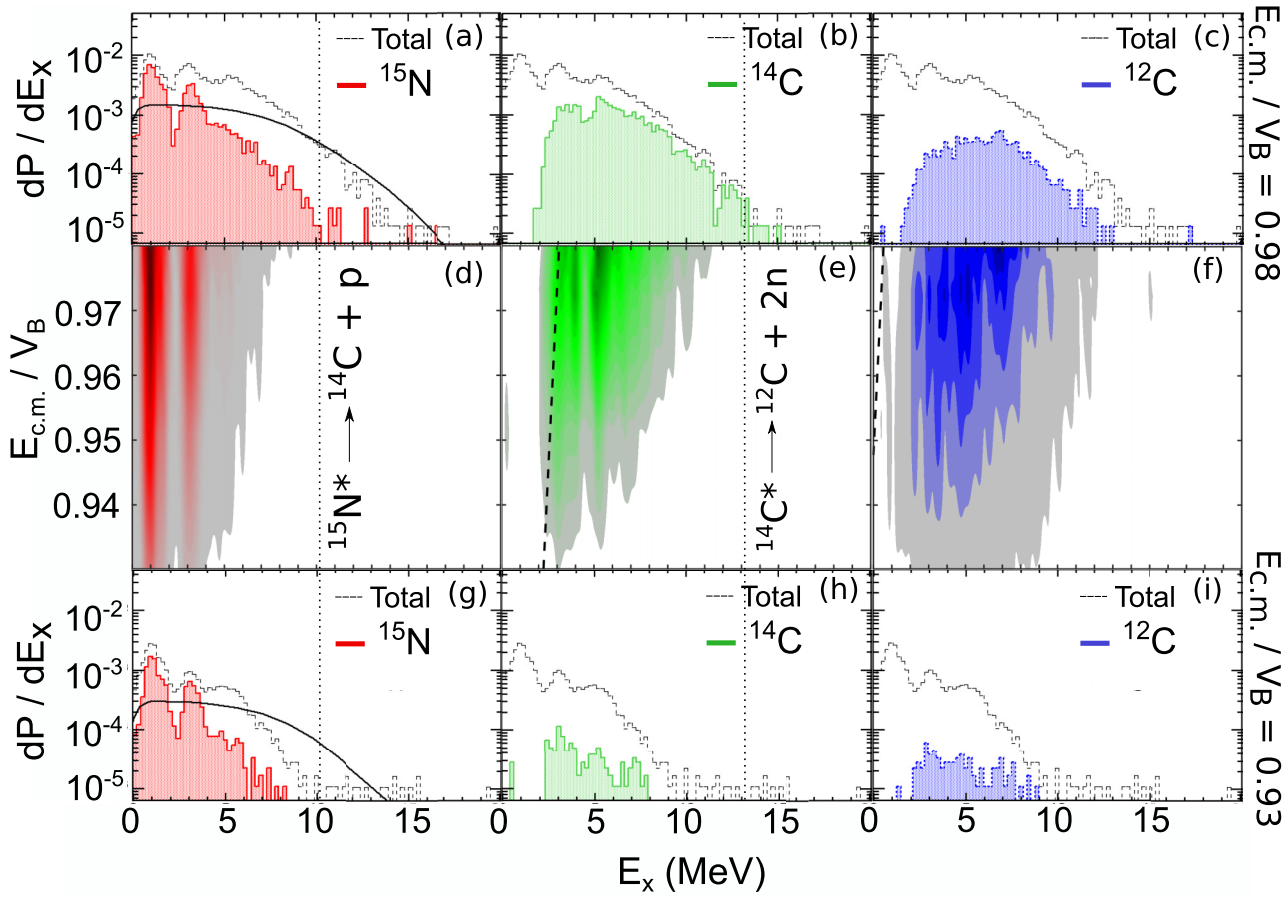

FIG. 11. (a–c) and (g–i) show the distribution of excitation energy in the $1p$, $2p$, and $2p2n$ channels (left to right) in the reaction ^{16}O + ^{208}Pb, measured relative to the ground state Q values for those processes, at bombarding energies of 73 MeV and 69.3 MeV, respectively (corresponding to $E_{c.m.}/V_B$ of 0.98 and 0.93). Black dashed line shows total excitation energy of all channels (including transfers and inelastic scattering). The filled areas show events corresponding to the detected product listed in the legend. The solid black curves in (a) and (g) show a GRAZING calculation [44] of the excitation energy for the single proton stripping channel. (d–f) are contour plots showing the distribution in excitation energy of each product as the beam energy varies relative to the Coulomb barrier energy. Contours are drawn in increments of 0.0001 in dP/dE_x. Thick black dashed line in (e) and (f) shows the evolution of the optimal excitation energy with bombarding energy, which is derived from the optimal Q value (see Appendix); in the case of the $1p$ stripping reaction shown in (d), the optimal Q value is less than $Q_{g.g.}$ and thus is not shown.

Figure 9(d) displays the $\Delta Z = -3$ modes, of which $-3p2n$ is very prominent. For comparison, the $-1p$ and $-2p2n$ trends are indicated by the blue solid and purple dash dotted lines, respectively. Transfer producing ^{14}C is almost as likely as $-2p2n$ at intermediate energies, before the $-3p2n$ probability falls off quickly at larger separations. The enhancement of the $-3p2n$ channel was found at higher energies in Ref. [43], which was interpreted as some kind of correlated p-α transfer. However, our results show that the ^{14}C yield is much diminished at the largest separations, and it seems that the behavior of this channel might also have a contribution from a more complex transfer + evaporation mechanism, as will be described in Sec. VI.

VI. EXCITATION ENERGY FOLLOWING TRANSFER

In the analysis of deep inelastic scattering, collision outcomes are generally characterized by the total kinetic energy loss (TKEL). Where the TKEL is large ($\gtrsim$100 MeV), the loss of kinetic energy resulting from the reduction of the Coulomb energy ΔV_C after charge stripping reactions is a small fraction of the total. In contrast, in the reactions studied here, ΔV_C often makes up the majority of the TKEL. If it were the ground states of the transfer products that were populated, the TKEL would be 25% of the total energy, or $\sim$15 MeV for a $\Delta Z = -2$ stripping reaction. However, such ground-state transfer should be treated in a coupled reaction channels approach in the same way as scattering populating any discrete states at low E_x.

In contrast, the population of high excitation energies with high level densities cannot practically be included explicitly in a coupled channels model space. This can be more closely related to both fusion in nucleon-nucleus collisions, and the classical treatment of energy loss in deep inelastic collisions (DICs). In both, an effectively irreversible coupling to a heat bath is implicit in the different treatments between fusion and energy loss in DICs, compared with peripheral scattering which is treated explicitly in a coherent quantum approach.

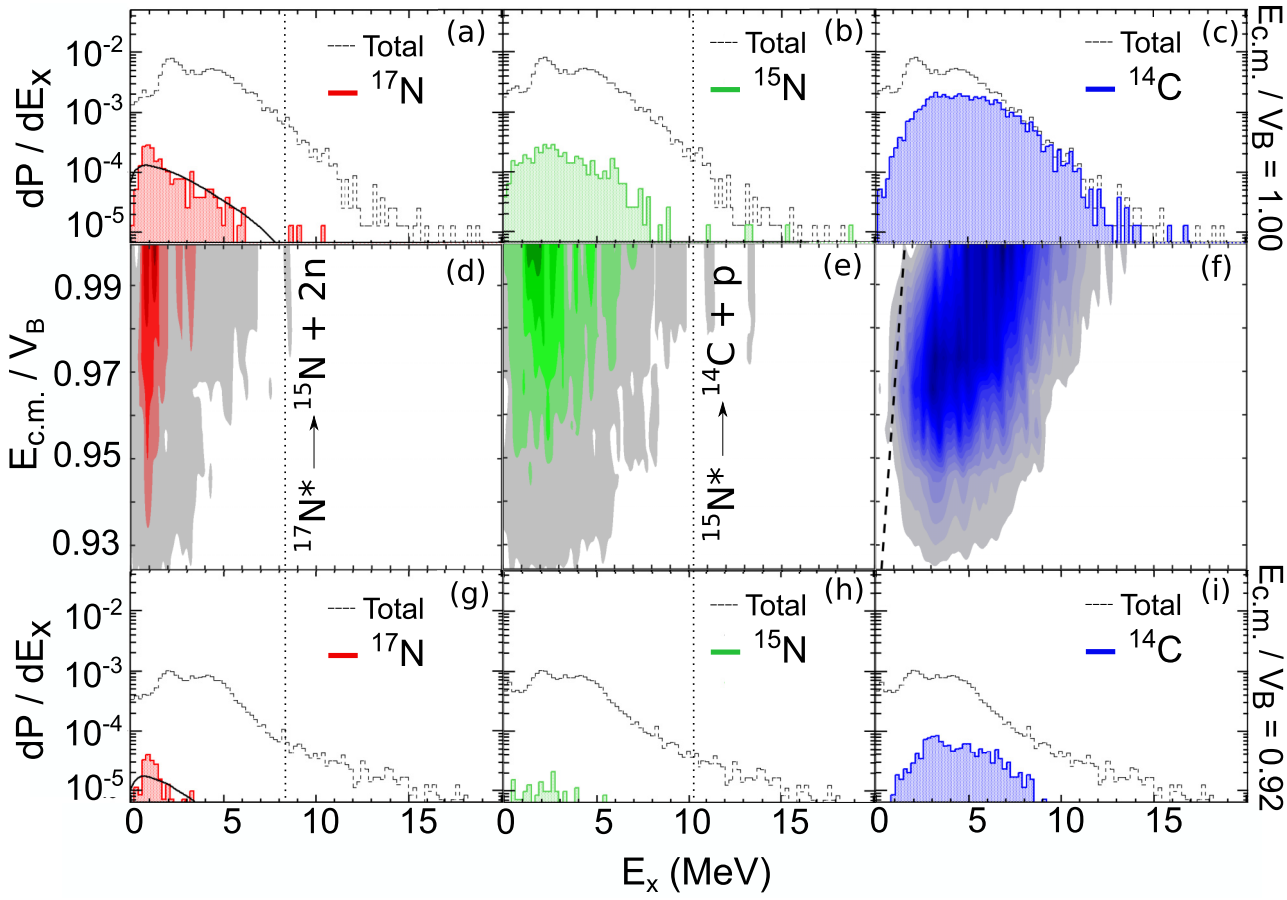

FIG. 12. (a–c) and (g–i) show the distribution of excitation energy in the $-1p$, $-1p2n$, and $-2p2n$ channels (left to right) in the reaction $^{18}\mathrm{O} + ^{208}\mathrm{Pb}$, measured relative to the ground state Q values for those processes, at bombarding energies of 73.6 MeV and 68 MeV, respectively (corresponding to $E_{\mathrm{c.m.}}/V_B$ of 1.00 and 0.92). The black dashed line shows total excitation energy of all channels (including transfers and inelastic scattering). The filled areas show events corresponding to the detected product listed in the legend. The solid black curves in (a) and (g) show a GRAZING calculation [44] of the excitation energy for the single proton stripping channel. (d–f) are contour plots showing the distribution in excitation energy of each product as the beam energy varies relative to the Coulomb barrier energy. Contours are drawn in increments of 0.0001 in dP/dE_x. Thick black dashed line in (f) shows the evolution of the optimal excitation energy with bombarding energy, which is derived from the optimal Q value (see Appendix); for modes shown in (d) and (e) the optimal Q value is below $Q_{\mathrm{g.g.}}$, and thus $E_{x\,\mathrm{opt}}$ is not visible.

Thus in this investigation of the crossover from quasielastic scattering to the energy dissipation seen in DICs, the excitation energy populated should be a more robust indicator of the likelihood of energy dissipation than TKEL. Accordingly we have carefully determined excitation energy distributions for each transfer mass partition, and their dependence on the internuclear separation.

Figure 10 shows the summed E_x distributions of all transfer modes for each reaction studied. Here the excitation energy is the sum for both the projectile-like and target-like fragments since our experiment cannot distinguish the partition of energy between the fragments. In general, the target-like fragment energies are expected to be larger, as is discussed below.

The general trend is for the distribution to extend to higher values of E_x as bombarding energy increases. Remarkably, even at the lowest beam energies, the measured distributions extend to ∼8 MeV for the oxygen projectiles (92% of V_B), and ∼10 MeV in the case of ^{19}F (90% of V_B).

In Figs. 11–13 we show the measured E_x distributions of the most significant charge transfer modes for the three reactions under study. We show the proportion of each mode compared to the total of all reaction products excluding the elastic scattering only. In each column the top and bottom panels show a high and low bombarding energy measurement, respectively. The central panel shows a contour plot of the evolution of these modes as the energy varies with respect to the barrier. These figures reiterate the observation that the system has a high excitation energy following transfer.

The overall distribution of excitation energy depends mainly upon two factors. Firstly, the probability for the transfer mode in question, which in turn depends upon the overlap of the Q window with the threshold for allowed states. Secondly, the density of states in the reaction products will determine how likely each is to reach a certain level of excitation [18]. The optimum Q value [defined in the Appendix, Eq. (A5)] can be transformed to an optimal E_x

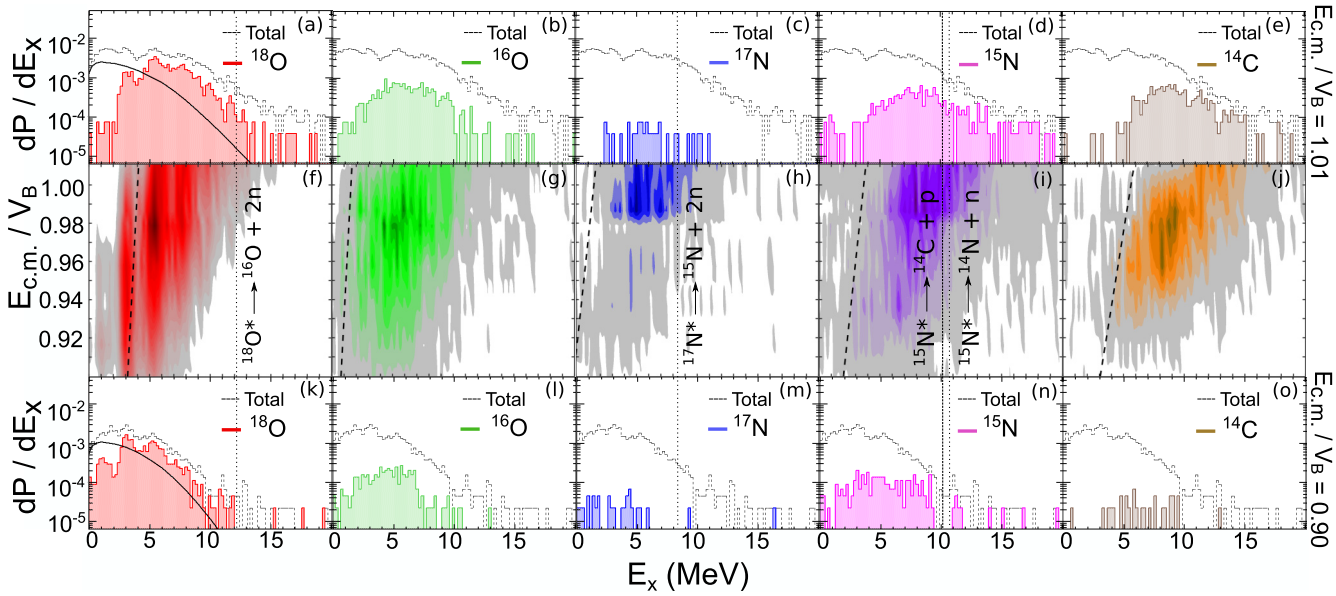

FIG. 13. (a–e) and (k–o) show the distribution of excitation energy in the $-1p$, $-1p2n$, $-2p$, $-2p2n$, and $-3p2n$ channels (left to right) in the reaction $^{19}\mathrm{F} + ^{208}\mathrm{Pb}$, measured relative to the ground state Q values for those processes, at bombarding energies of 83.3 MeV and 74.1 MeV, respectively (corresponding to $E_{\mathrm{c.m.}}/V_B$ of 1.01 and 0.90). The black dashed lines show total excitation energy of all channels (including transfers and inelastic scattering). The filled areas show events corresponding to the detected product listed in the legend. The solid black curves in (a) and (k) show a GRAZING calculation [44] of the excitation energy for the single proton stripping channel. (f–j) are contour plots showing the distribution in excitation energy of each product as the beam energy varies relative to the Coulomb barrier energy. Contours are drawn in increments of 0.0001 in dP/dE_x. Thick black dashed line shows the evolution of the optimal excitation energy with bombarding energy, which is derived from the optimal Q value (see Appendix).

by subtracting the ground-state Q value for the channel in question, i.e., $E_{x\,\mathrm{opt}} = Q_{\mathrm{opt}} - Q_{g.g.}$. In the central panels of each column in Figs. 11–13, the thick dashed black lines show the evolution of $E_{x\,\mathrm{opt}}$ with beam energy, moving to higher E_x values with higher bombarding energy. Where these lines are not visible, the optimum Q value lies below $Q_{g.g.}$. These modes are generally suppressed compared to those in which $E_{x\,\mathrm{opt}}$ reaches significant positive values.

Figures 11–13 show that although all channels qualitatively follow the systematics expected from optimum Q-value considerations, there are distinct differences in the E_x distributions between multinucleon transfer channels and those in which only a single nucleon is transferred. While single proton transfer leads to a distribution exhibiting regions of low and high population, suggesting the population of well-defined discrete states, the distributions of multinucleon transfer processes have higher mean E_x, and are essentially featureless. This suggests that there are a large number of states populated in these processes. Even at the lowest bombarding energies, there remains a spread in E_x over 10 MeV for these channels. This flags the possible beginning of dissipative processes even at large internuclear separation.

We can generally discount evaporation from an excited projectile-like nucleus as significantly distorting our measured transfer probabilities. Various evaporation thresholds are indicated in Figs. 11–13. Only in the case of the $^{208}\mathrm{Pb}(^{19}\mathrm{F},^{15}\mathrm{N})^{212}\mathrm{Po}$ measurement [Figs. 13(d), 13(i), and 13(n)] is there a significant distribution of E_x above the nucleon emission thresholds, and there is no sign of a discontinuity in this region that might be expected from these processes. There may be a contribution to the yield of ^{15}N in the $^{19}\mathrm{F} + ^{208}\mathrm{Pb}$ reaction due to neutron evaporation from ^{16,17}N transfer products due to their relatively low neutron separation energies. However, the Q values for producing ^{16,17}N are unfavorable, and in general we expect this contribution to be low. Similar arguments cannot explain the very strong production of ^{14}C in the $^{18}\mathrm{O} + ^{208}\mathrm{Pb}$ case.

Since excitations can occur in both the target and projectile, the thresholds so determined represent absolute minima. It is likely that the target-like product will carry most of the excitation energy due to its higher level density at a given excitation energy. Most of the channels observed are those in which the heavy partner receives the transferred nucleons [24], which has been shown to be important in determining the collision partner that becomes excited in the transfer process [45,46].

We also show excitation energy distributions from the code GRAZING [44] for one-proton stripping, which is based on the semiclassical approximation and makes use of empirical form factors for single particle transfer. This code can calculate the distribution of excitation energy E_x between the projectile and target in heavy ion transfer reactions, and is shown in Figs. 11–13 to have varying success in predicting the measured excitation energy distributions for single proton stripping reactions. The GRAZING prediction for the E_x-integrated probability is generally higher than that measured, and the calculation shown in the frame has been renormalized to the measured value. The extent of the E_x distribution is significantly overpredicted in the case of $^{16}\mathrm{O} + ^{208}\mathrm{Pb}$, where

we in fact observe a concentration of E_x in well-defined states at lower energy. The agreement for the ^{18}O and ^{19}F induced reactions is generally good, though at the highest energies in the case of ^{19}F, the distribution is peaked at more positive values than predicted by GRAZING.

VII. CONCLUSIONS AND OUTLOOK

In this work we have reported new experimental results for multinucleon transfer channels and their associated excitation energy in ^{16,18}O and ^{19}F induced reactions on a ^{208}Pb target at a series of sub-barrier energies. Many different transfer products emerge from each reaction, even at the lowest bombarding energies. The dominant transfer modes vary widely between the different projectiles, despite their proximity in the nuclear chart. The observed transfer probabilities are driven to a large extent by Q-value considerations.

The relative importance of the different transfer channels in each system is shown to vary significantly with the internuclear separation. For example, our results suggest that at low energy, when the internuclear distance is large, an extensive α-cluster configuration of ^{16}O might be preferentially probed over the configurations contributing to the $2p$ transfer channel. With ^{18}O, α-stripping is by far the strongest mode at near barrier energies, but is weaker than both $1n$ and $2n$ stripping at large separations.

Distinctions can be drawn between those reactions involving single nucleon transfer and those that involve the transfer of many nucleons. The former leads to a strong population of states at low excitation energies, while the latter involves the excitation energy being distributed over very many states, and extending to high excitation energies. Coupled-channels models often only consider transfer to low lying, strongly populated states. Our results show such processes are only a small part of the total, and that a broad range of excited states in the products are populated via multinucleon transfer. As more nucleons are transferred, the mean excitation energy grows.

The significant probabilities for transfer reactions in ^{16,18}O, ^{19}F + ^{208}Pb, even at beam energies below the fusion barriers, combined with the observed population of excitation energies of 10 MeV and more, imply the dissipation of kinetic energies. These observations strengthen the case that energy dissipation may play a significant role in fusion hindrance even for projectiles as light as ^{16}O. A quantitative model to estimate the effect of (multi)nucleon transfer on fusion is required to take this idea further.

ACKNOWLEDGMENTS

The authors wish to thank the technical staff of the ANU Heavy Ion Accelerator Facility for their support during the experiment. Thanks are also given to M. Evers for discussions and contributions to the analysis code developed for use with the new detector, as well as input to the early planning stages of the experiment. This work was supported by Australian Research Council Grants No. DP120101569, No. FT120100760, and No. FL110100098.

APPENDIX: SEMICLASSICAL THEORY OF TRANSFER

The semiclassical description of transfer [31] treats the relative motion of the colliding system classically and the transfer process quantum mechanically. In the first-order Born approximation, the transfer probability to state β with Q-value Q_β can be written in the form

$$P_{\rm Tr}(r_{\rm min}, Q_\beta) = \frac{\pi}{\sigma^2}|F_\beta(r_{\rm min}, Q_\beta)|^2 g(Q_\beta), \tag{A1}$$

where $F_\beta(r_{\rm min}, Q_\beta)$ is the transfer form factor, and $r_{\rm min}$ is the distance of closest approach. This can be calculated in the low energy limit [31] by

$$r_{\rm min} = \frac{Z_p Z_t e^2}{4\pi\epsilon_0}\frac{1}{2E_{\rm c.m.}}\left(1+\csc\frac{\theta_{\rm c.m.}}{2}\right). \tag{A2}$$

This is a standard and convenient way of representing the energy dependence of transfer cross sections [15]. Of course, the transfer occurs over the whole trajectory, including either the incoming or outgoing trajectories, before and after the point of closest approach. The observed transfer probability is thus an integral over the whole trajectory.

The factor $g(Q_\beta)$ is the adiabatic cutoff function which defines the Q window (i.e., the range of kinematically favorable states produced in the reaction):

$$g(Q_\beta) = \exp\left(\frac{-(Q_\beta - Q_{\rm opt})^2}{2\sigma^2}\right). \tag{A3}$$

Here, the width of the distribution is estimated by

$$\sigma = \sqrt{\frac{\alpha\hbar^2\ddot{r}}{2}}, \tag{A4}$$

where $\ddot{r}$ is the acceleration of the projectile at the distance of closest approach [47]. The optimum Q value, $Q_{\rm opt}$, can be calculated based on the requirement that the classical trajectories join smoothly in the entrance and exit channels [48]:

$$Q_{\rm opt} = E_{\rm c.m.}\left[\left(\frac{Z_3 Z_4}{Z_1 Z_2}\right) - 1\right], \tag{A5}$$

using the same notation as Eq. (1). It is worth mentioning that there have been several different formulations of the optimum Q value [49–52]. The above simple expression does not include the effect of target recoil, though at these low energies and with such projectiles relative to the target mass, these effects can be considered negligible.

Assuming equal probability for all excited states, integrating Eq. (A1) with respect to Q gives the total transfer probability for each mass partition:

$$P(r_{\rm min}) = \frac{\pi}{\sigma^2}|F(r_{\rm min})|^2\int_{-\infty}^{Q_{\rm g.g.}}\rho(Q)\exp\left(-\frac{(Q-Q_{\rm opt})^2}{2\sigma^2}\right)dQ, \tag{A6}$$

where $\rho\,(Q)$ is the level density. The form factor now becomes the Q-independent $F\,(r_{\rm min})$, which is normally parametrized as

$$F(r_{\rm min}) = F_0\exp(-2\alpha r_{\rm min}). \tag{A7}$$

TABLE II. Ground-state–to–ground-state $Q_{\text{g.g.}}$ and effective ($Q_{\text{g.g}} + \Delta V_C$) Q values for various transfer processes in the systems studied here, as well as theoretical slope parameters α_{Th} and experimental α_{exp} where it has been possible to extract them. P_{Tr} are those measured at separations of 13.41, 13.51, and 13.55 fm for the ^{16}O + ^{208}Pb, ^{18}O + ^{208}Pb, ^{19}F + ^{208}Pb systems, respectively, corresponding to ≈95% V_B. ΔV_C were calculated at these separations.

System	Transfer channel	Product	$Q_{\text{g.g.}}$ (MeV)	$Q_{\text{g.g.}} - \Delta V_C$	P_{Tr}	α_{Calc} (fm^{-1})[a]	α_{exp} (fm^{-1})
^{16}O + ^{208}Pb	+1p	^{17}F	− 7.403	− 15.241	−	0.699	−
	+2n	^{18}O	− 1.917	− 1.917	0.0079 ± 0.0033	1.153	1.376 ± 0.301
	+1n	^{17}O	− 3.224	− 3.224	0.0306 ± 0.0062	0.594	0.704 ± 0.153
	−1n	^{15}O	− 11.726	− 11.726	−	0.605	−
	−2n	^{14}O	− 19.764	− 19.764	−	1.187	−
	−1p	^{15}N	− 8.328	− 0.275	0.0266 ± 0.0009	0.714	1.160 ± 0.036
	−1p1n	^{14}N	− 14.557	− 6.250	−	1.291	−
	−1p2n	^{13}N	− 19.972	− 12.670	−	1.842	−
	−2p	^{14}C	− 13.552	2.769	0.0078 ± 0.0005	1.380	2.374 ± 0.065
	−2p1n	^{13}C	− 17.178	− 0.856	0.0009 ± 0.0001	1.929	2.608 ± 0.247
	−2p2n	^{12}C	− 16.116	0.205	0.0042 ± 0.0003	2.451 (2.016)	1.730 ± 0.085
^{18}O + ^{208}Pb	+1p	^{19}F	− 0.010	− 7.790	−	0.702	−
	+1n	^{19}O	− 3.412	− 3.412	0.0166 ± 0.0018	0.589	1.143 ± 0.913
	−1n	^{17}O	− 4.108	− 4.108	0.0162 ± 0.0013	0.602	0.629 ± 0.460
	−2n	^{16}O	− 3.065	− 3.065	0.0155 ± 0.0009[b]	1.184	1.178 ± 0.170
	−1p	^{17}N	− 12.143	− 4.153	0.0011 ± 0.0002	0.711	1.491 ± 0.169
	−1p1n	^{16}N	− 13.423	− 5.433	0.0005 ± 0.0001	1.288	1.753 ± 0.224
	−1p2n	^{15}N	− 10.774	− 2.784	0.0028 ± 0.0003	1.842	2.198 ± 0.122
	−2p	^{16}C	− 20.272	− 4.073	−	1.378	−
	−2p1n	^{15}C	− 19.971	− 3.772	−	1.930	−
	−2p2n	^{14}C	− 15.182	1.017	0.0270 ± 0.0010	2.459 (2.006)	2.734 ± 0.007
	−2p3n	^{13}C	− 19.002	− 2.803	0.0018 ± 0.0004	2.965	3.329 ± 0.046
	−2p4n	^{12}C	− 18.061	− 1.862	0.0004 ± 0.0002	3.449	3.088 ± 0.067
	−3p4n	^{11}B	− 29.943	− 5.447	−	3.972	−
^{19}F + ^{208}Pb	+1p2n	^{22}Ne	+8.609	0.957		1.803	
	+1p1n	^{21}Ne	+4.749	− 2.903	0.0018 ± 0.0003[c]	1.268	0.717 ± 0.152[d]
	+1p	^{20}Ne	+4.839	− 2.813		0.707	
	+1n	^{20}F	− 0.766	− 0.766	0.0604 ± 0.0120	0.593	0.815 ± 0.082
	+2n	^{21}F	0.597	0.597	−	1.156	−
	−1n	^{18}F	− 6.494	− 6.494	−	0.603	−
	−1p	^{18}O	− 4.195	3.496	0.1024 ± 0.0079	0.711	0.647 ± 0.065
	−1p1n	^{17}O	− 7.635	0.055	0.0099 ± 0.0053	1.290	0.733 ± 0.414
	−1p2n	^{16}O	− 6.640	1.050	0.0246 ± 0.0037	1.847	1.021 ± 0.120
	−2p	^{17}N	− 15.153	0.48	0.0007 ± 0.0002	1.380	1.212 ± 0.446
	−2p1n	^{16}N	− 16.487	− 0.857	0.0004 ± 0.0002	1.935	1.315 ± 0.307
	−2p2n	^{15}N	− 12.968	3.357	0.0088 ± 0.0008	2.468 (1.956)	0.677 ± 0.270
	−3p2n	^{14}C	− 19.676	4.024	0.0118 ± 0.0009	3.054	1.999 ± 0.397
	−3p3n	^{13}C	− 22.981	0.719	0.0001 ± 0.0001	3.540	2.280 ± 2.705
	−3p4n	^{12}C	− 21.980	1.720	0.0005 ± 0.0002	4.003	2.581 ± 0.133

[a]For the −2p2n channels in each reaction, we have given α_{Th} in brackets where it has been calculated using Q_α as the effective binding energy.
[b]The 2n stripping channel of ^{18}O + ^{208}Pb is likely underestimated slightly as these events are obscured by the elastically scattered particles.
[c]We cannot distinguish between the neon isotopes, so it is unknown if the yield corresponds to a single isotope or several.
[d]slope in this case is extracted from the mass integrated $Z = 10$ events.

The parameter $\alpha = \frac{\sqrt{2\mu E_b}}{\hbar}$ is known as the slope parameter, in which μ is the reduced mass and E_b is the binding energy of the nucleons being transferred. For neutrons, which are not influenced by the Coulomb field, E_b in this expression is taken as the normal binding energy, where protons are transferred the effects of the Coulomb field of the approaching collision partner must be taken into account as well as the barrier that must be overcome by the transferred protons, and as such an effective binding energy is used [53]. When considering the possibility of clusters of nucleons being transferred, the effective binding energy for the cluster should be used in the calculation. In addition, α is calculated as the average of the slopes in the donor and acceptor nuclei [47]:

$$\alpha = \tfrac{1}{2}(\alpha_1 + \alpha_2). \tag{A8}$$

Here, the 1 and 2 indices indicate the donor and acceptor, respectively. The α values as calculated in this manner (α_{calc}, as well as those extracted from the data shown in Figs. 7–9 (α_{exp}) are listed in Table II.

[1] C. H. Dasso, S. Landowne, and A. Winther, Nucl. Phys. A **405**, 381 (1983).
[2] K. Hagino and N. Takigawa, Prog. Theor. Phys. **128**, 1061 (2012).
[3] M. Dasgupta, D. J. Hinde, N. Rowley, and A. M. Stefanini, Annu. Rev. Nucl. Part. Sci. **48**, 401 (1998).
[4] H. Esbensen, C. L. Jiang, and A. M. Stefanini, Phys. Rev. C **82**, 054621 (2010).
[5] M. Evers, M. Dasgupta, D. J. Hinde, L. R. Gasques, M. L. Brown, R. Rafiei, and R. G. Thomas, Phys. Rev. C **78**, 034614 (2008).
[6] J. O. Newton, R. D. Butt, M. Dasgupta, D. J. Hinde, I. I. Gontchar, C. R. Morton, and K. Hagino, Phys. Lett. B **586**, 219 (2004).
[7] M. Dasgupta, D. J. Hinde, A. Diaz-Torres, B. Bouriquet, C. I. Low, G. J. Milburn, and J. O. Newton, Phys. Rev. Lett. **99**, 192701 (2007).
[8] J. O. Newton, R. D. Butt, M. Dasgupta, D. J. Hinde, I. I. Gontchar, C. R. Morton, and K. Hagino, Phys. Rev. C **70**, 024605 (2004).
[9] G. Pollarolo, Nucl. Phys. A **787**, 206 (2007).
[10] C. L. Jiang, K. E. Rehm, B. B. Back, and R. V. F. Janssens, Phys. Rev. C **79**, 044601 (2009).
[11] H. Esbensen and Ş. Mişicu, Phys. Rev. C **76**, 054609 (2007).
[12] C. H. Dasso and G. Pollarolo, Phys. Rev. C **39**, 2073 (1989).
[13] T. Ichikawa and K. Matsuyanagi, Phys. Rev. C **88**, 011602(R) (2013).
[14] K. E. Rehm, A. M. van den Berg, J. J. Kolata, D. G. Kovar, W. Kutschera, G. Rosner, G. S. F. Stephans, and J. L. Yntema, Phys. Rev. C **37**, 2629 (1988).
[15] K. E. Rehm, Annu. Rev. Nucl. Part. Sci. **41**, 429 (1991).
[16] A. Diaz-Torres, D. J. Hinde, M. Dasgupta, G. J. Milburn, and J. A. Tostevin, Phys. Rev. C **78**, 064604 (2008).
[17] M. Evers, M. Dasgupta, D. J. Hinde, D. H. Luong, R. Rafiei, R. du Rietz, and C. Simenel, Phys. Rev. C **84**, 054614 (2011).
[18] L. Corradi, G. Pollarolo, and S. Szilner, J. Phys. G: Nucl. Part. Phys. **36**, 113101 (2009).
[19] J. F. Ziegler, M. D. Ziegler, and J. P. Biersack, Nucl. Instrum. Methods Phys. Res. B **268**, 1818 (2010).
[20] C. R. Morton, A. C. Berriman, M. Dasgupta, D. J. Hinde, J. O. Newton, K. Hagino, and I. J. Thompson, Phys. Rev. C **60**, 044608 (1999).
[21] G. F. Knoll, *Radiation Detection and Measurement* (John Wiley & Sons, New York, 2010).
[22] L. R. Gasques, M. Evers, D. J. Hinde, M. Dasgupta, P. R. S. Gomes, R. M. Anjos, M. L. Brown, M. D. Rodríguez, R. G. Thomas, and K. Hagino, Phys. Rev. C **76**, 024612 (2007).
[23] A. G. Artukh, V. V. Avdeichikov, J. Erö, G. F. Gridnev, V. L. Mikheev, V. V. Volkov, and J. Wilczynski, Nucl. Phys. A **160**, 511 (1971).
[24] V. V. Volkov, Phys. Rep. **44**, 93 (1978).
[25] V. I. Zagrebaev, Phys. Rev. C **67**, 061601(R) (2003).
[26] A. V. Karpov, V. A. Rachkov, and V. V. Samarin, Phys. Rev. C **92**, 064603 (2015).
[27] W. Von Oertzen and A. Vitturi, Rep. Prog. Phys. **64**, 1247 (2001).
[28] T. Härtlein, H. Bauer, D. Pansegrau, and D. Schwalm, Eur. Phys. J. A **4**, 41 (1999).
[29] F. W. N. Boer, H. J. Wollersheim, H. Emling, H. Grein, E. Grosse, W. Spreng, G. Eckert, T. W. Elze, K. Stelzer, and C. Lauterbach, Z. Phys. A **325**, 457 (1986).
[30] A. E. S. Green, Phys. Rev. **95**, 1006 (1954).
[31] R. A. Broglia and A. Winther, *Heavy Ion Reactions* (Benjamin-Cummings, San Francisco, 1991).
[32] C. Simenel, Phys. Rev. Lett. **105**, 192701 (2010).
[33] G. Scamps and D. Lacroix, Phys. Rev. C **87**, 014605 (2013).
[34] C. Simenel, Phys. Rev. Lett. **106**, 112502 (2011).
[35] C. Simenel, Eur. Phys. J. A **48**, 1 (2012).
[36] K. Sekizawa and K. Yabana, Phys. Rev. C **88**, 014614 (2013).
[37] F. Videbæk, R. B. Goldstein, L. Grodzins, S. G. Steadman, T. A. Belote, and J. D. Garrett, Phys. Rev. C **15**, 954 (1977).
[38] M. A. Franey, J. S. Lilley, and W. R. Phillips, Nucl. Phys. A **324**, 193 (1979).
[39] E. Vulgaris, L. Grodzins, S. G. Steadman, and R. Ledoux, Phys. Rev. C **33**, 2017 (1986).
[40] C. Simenel and B. Avez, Int. J. Mod. Phys. E **17**, 31 (2008).
[41] P. R. Christensen, V. I. Manko, F. D. Becchetti, and R. J. Nickles, Nucl. Phys. A **207**, 33 (1973).
[42] D. C. Biswas, P. Roy, Y. K. Gupta, B. N. Joshi, B. K. Nayak, L. S. Danu, B. V. John, R. P. Vind, N. Deshmukh, S. Mukherjee, A. K. Jain, and R. K. Choudhury, J. Phys.: Conf. Ser. **381**, 012091 (2012).
[43] D. C. Biswas, R. K. Choudhury, B. K. Nayak, D. M. Nadkarni, and V. S. Ramamurthy, Phys. Rev. C **56**, 1926 (1997).
[44] A. Winther, Nucl. Phys. A **572**, 191 (1994).
[45] K. Sekizawa and K. Yabana, Phys. Rev. C **93**, 054616 (2016).
[46] S. B. Gazes, H. R. Schmidt, Y. Chan, E. Chavez, R. Kamermans, and R. G. Stokstad, Phys. Rev. C **38**, 712 (1988).
[47] S. Saha, Y. K. Agarwal, and C. V. K. Baba, Phys. Rev. C **49**, 2578 (1994).
[48] P. J. A. Buttle and L. J. B. Goldfarb, Nucl. Phys. A **176**, 299 (1971).
[49] J. Wilczyński, Phys. Lett. B **47**, 124 (1973).
[50] J. P. Schiffer, H. J. Körner, R. H. Siemssen, K. W. Jones, and A. Schwarzschild, Phys. Lett. B **44**, 47 (1973).
[51] J. Wilczynski and H. W. Wilschut, Phys. Rev. C **39**, 2475 (1989).
[52] D. M. Brink, Phys. Lett. B **40**, 37 (1972).
[53] L. Corradi, S. J. Skorka, U. Lenz, K. E. G. Lãbner, P. R. Pascholati, U. Quade, K. Rudolph, W. Schomburg, M. Steinmayer, H. G. Thies, G. Montagnoli, D. R. Napoli, A. M. Stefanini, A. Tivelli, S. Beghini, F. Scarlassara, C. Signorini, and F. Soramel, Z. Phys. A **335**, 55 (1990).